Journal of Alloys and Compounds 966 (2023) 171640

Contents lists available at ScienceDirect

Journal of Alloys and Compounds

journal homepage: www.elsevier.com/locate/jalcom

Silver-induced γ→ε martensitic transformation in FeMn alloys: An experimental and computational study

Aleksandra Bartkowska[a,*], Christina E. Lekka[b,*], Ludovico Andrea Alberta[c], Irena Spasojevic[a], Eva Pellicer[a], Jordi Sort[a,d,**]

[a] Departament de Física, Universitat Autònoma de Barcelona, Bellaterra, E-08193 Cerdanyola del Vallès, Spain
[b] Department of Materials Science and Engineering, University of Ioannina, 45110 Ioannina, Greece
[c] Leibniz Institute for Solid State and Materials Research Dresden (IFW Dresden), Helmholtzstr. 20, D-01069 Dresden, Germany
[d] Institució Catalana de Recerca i Estudis Avançats (ICREA), Pg. Lluís Companys 23, E-08010 Barcelona, Spain

ARTICLE INFO

Keywords:
Iron-manganese alloys
Austenite
Martensite
Silver
Magnetic properties
Phase transformation

ABSTRACT

Porous FeMn alloys with additions of 0, 1, 3 and 5 wt% of Ag were fabricated using powder metallurgy and sintering. The microstructure of the fabricated alloys was characterized using X-ray diffraction, transmission electron microscopy and selected area electron diffraction. While equiatomic FeMn and FeMn-1Ag alloys possess a fully austenitic structure, a change in the crystallographic structure is observed upon addition of 3 and 5 wt% of Ag, where a mixture of γ austenite and ε martensite phases is observed. Compression tests reveal that such structural transition causes an increase of the yield stress. The evolution of microstructure with the Ag content can be understood from theoretical calculations which show that Ag atoms prefer the intrinsic stacking fault (ISF) sites, revealing lower energy for the ε atomic plane sequence. This causes local depletion of the electronic charge, therefore weakening the interatomic bonds at the ISF plane and facilitating the phase transition. In addition, the total energy difference between the γ and ε phases decreases upon Ag addition. This enables the coexistence of both phases in the sample with 5 wt% Ag. Both experimental and theoretical data agree that the magnetization value gradually increases upon Ag addition. This is due to the local stress that is introduced by Ag atoms, which expand the Ag-Fe and Ag-Mn first neighbour interatomic bonds compared to FeMn. This stress results in electronic charge transfer that locally alters the Fe and Mn atomic magnetic moments. These results are appealing for the design of FeMn-based alloys with tuneable phase composition and physical properties for several technological applications.

1. Introduction

Fe-Mn alloys have been studied as versatile materials in widespread applications such as steels for automotive applications [1,2], antiferromagnetic layers in spin valves [3,4], or biodegradable metals for implant applications [5–7], amongst others. The solid solution phases characteristic of the Fe-Mn system are γ-austenite, α-ferrite, δ-Fe, α-Mn, β-Mn and δ-Mn. Moreover, a metastable hexagonally close-packed (hcp) ε phase can be formed by martensitic transformation in alloys with Mn content above 10 wt%. This transformation can occur owing to prior deformation, high applied pressure or fast cooling from the liquid state by the movement of Shockley partial dislocations between Fe and Mn on the $(111)_\gamma$ plane [8]. The γ→ε phase transformation is strongly associated with the stacking fault energy [8,9]. It has been shown that a low stacking fault energy, below 20 mJ m^{-2}, facilitates the transformation of fcc γ-austenite into hcp ε-martensite [10]. The stacking fault energy can be affected by several factors, such as defects or the addition of elements. For example, additions of Al strongly suppress the phase transformation, as they increase the stacking fault energy of γ-austenite [11]. In contrast, the addition of Si lowers the stacking fault energy, favoring the γ→ε phase transformation [12]. Several *ab initio* calculations on Fe reveal that the presence of Mn or C causes a minimum in the stacking fault energy (around -450 mJ m^{-2} for Fe), thus favoring the ε phase [13–15].

Depending on the crystallographic phase, Fe-Mn alloys can find potential use in different areas of materials science. For instance,

---

* Corresponding authors.
** Corresponding author at: Departament de Física, Universitat Autònoma de Barcelona, Bellaterra, E-08193 Cerdanyola del Vallès, Spain.
E-mail addresses: Aleksandra.Bartkowska@uab.cat (A. Bartkowska), chlekka@uoi.gr (C.E. Lekka), jordi.sort@uab.cat (J. Sort).

https://doi.org/10.1016/j.jallcom.2023.171640
Received 7 June 2023; Received in revised form 20 July 2023; Accepted 2 August 2023

γ-$Fe_{50}Mn_{50}$ alloys are the basis of antiferromagnetic metallic pinning layers used in spin valves or magnetic tunnel junction devices [16]. High-manganese steels, which show mostly austenitic fcc structure, are known for their high strength and ductility, owing to their high strain hardening capacity [17]. These steels, typically comprising high Mn contents ($>$ 20 wt%) and additions of C ($<$ 1 wt%), Si ($<$ 3 wt%) and Al ($<$ 10 wt%), exhibit various hardening mechanisms, such as twinning-induced plasticity (TWIP) and transformation-induced plasticity (TRIP). The TWIP effect is observed in steels with low stacking fault energy, between 20 and 40 mJ m^{-2} [17] and it relies on the transformation of retained austenite into martensite during plastic deformation, which enhances both strength and ductility [2]. Furthermore, in recent years, Fe-based alloys (including Fe-Mn) have emerged as potential candidates for biodegradable materials applications [5,6,18]. Biodegradable alloys are a new class of implantable materials that aim to gradually degrade *in vivo* until their role is fulfilled, without the need for an implant removal operation. This is important to limit the cost of medical treatment and to reduce patients' morbidity. Owing to the high mechanical strength of iron, these alloys surpass the mechanical properties of other biodegradable biomaterials, such as polymers, or Mg- and Zn-based alloys. In the last decade, manganese was established as suitable alloying element in Fe-based biodegradable alloys, since a high content of Mn stabilizes the austenite phase which exhibits antiferromagnetic properties, thus making this material compatible with magnetic resonance imaging (MRI) [7,18–23]. In addition, alloys with various amounts of Mn demonstrate good mechanical properties, a degradation rate higher than in pure Fe, and good cytocompatibility [18,19,23,24].

Due to the extensive use of artificial implant materials, implant-associated bacterial infections have become increasingly common because of biofilm formation, adhesion, and colonization of bacteria on the implant surface [25,26]. Therefore, there is a need to develop materials with antibiofilm and antibacterial properties. Among other strategies, addition of Ag has been extensively tested and proven efficient in promoting antibacterial properties [27,28]. Besides preventing the biofilm formation on the material surface [7], the addition of Ag to the Fe-Mn system has several advantages such as accelerating short-term corrosion [29] or increasing the strength [30]. In fact, the solubility of Ag in γ-austenite is below 0.4 at% [31], therefore the formation of Ag-rich precipitates is expected. These precipitates can act as micro-galvanic cells [29], which help increase the corrosion rate of Fe-based alloys.

Interestingly, reports on FeMn-Ag alloys have shown that additions of Ag favor the formation of the martensitic phase, although so far this effect has not been understood or described in detail. For example, in the Fe30Mn-Ag alloys reported by Liu et al. [32], the content of the ε phase increased upon the addition of Ag. In another study by Babacan et al. [33], Ag-bearing alloys showed a higher content of martensite than alloys without Ag. Similar observations were described by Dehghan-Manshadi et al. [34], where additions of Ag increased the intensity of the ε-martensite peaks in diffraction measurements. Hence, besides providing antibacterial properties, addition of Ag to Fe-Mn can lead to microstructural changes that improve the compressive yield strength of the alloy. However, the effect of added Ag on the structure and the mechanical and magnetic properties of Fe-Mn alloys has been largely overlooked.

In this work, we investigate the phase transformation from austenite to martensite induced in Fe-Mn alloys by the addition of 1 – 5 wt% Ag. We also correlate the changes in microstructure with the mechanical and magnetic properties of the resulting alloys. Moreover, a theoretical study is conducted to understand the phase transformation and the alterations of the magnetic properties of FeMn due to the presence of Ag, mainly associated to a charge transfer and alterations in the first neighbor's atomic magnetic moments.

2. Materials and methods

2.1. Sample preparation and characterization

Iron-manganese equiatomic alloys with varying content of Ag (0, 1, 3 and 5 wt%, denoted as FeMn, FeMn-1Ag, FeMn-3Ag and FeMn-5Ag, respectively) were fabricated using powder metallurgy techniques, namely ball milling of commercial Fe (>99% purity), Mn (>99% purity) and Ag (>99.9% purity) powders in a planetary ball mill for 10 h and subsequent sintering under vacuum at 900 °C, as described in our previous report [7]. X-ray diffraction (XRD) was performed on polished surfaces of all tested alloys to assess the phase composition. The experiments were performed on a Panalytical X′Pert powder diffractometer with Cu K_α radiation, in the angular range between 20° and 100° and a step size of 0.026° in the Bragg-Brentano geometry.

Thin lamellae of FeMn and FeMn-5Ag samples were prepared for transmission electron microscopy (TEM) observations by focused ion beam (FIB). The microstructure images and selected-area diffraction (SAED) patterns were acquired using a Jeol 2011 TEM operating at 200 kV. High-resolution images were also obtained by scanning-transmission electron microscopy (STEM) utilizing a Teknai Fei instrument operating at 200 kV. The SAED patterns were indexed by the Gatan Digital Micrograph software, which was also employed to analyze the high-resolution images and the corresponding fast Fourier transform (FFT) images. From the SAED patterns and the FFT, the interplanar distances were obtained as well as the lattice constants.

The mechanical properties of the alloys were assessed through compression testing. Specimens of cylindrical shape were prepared according to *DIN 50106:2016–11* with a height (4 mm) to diameter (2 mm) ratio of 2. Loading surfaces were ground with silicon carbide papers to become plane parallel. Uniaxial compression tests were performed at room temperature using an Instron 8562 device at a constant strain rate of 1×10^{-3} s^{-1} and at least three specimens per composition were tested. The tests were halted at fracture. The following mechanical properties were determined from the engineering stress-strain compression curves: compressive yield strength (proof offset 0.2%, $R_{0.2}$), compressive ultimate strength (R_m) and compressive strain (A).

To assess magnetic properties, hysteresis loops were recorded at room temperature using a vibrating sample magnetometer (VSM, MicroSense). The maximum applied magnetic field was 20 kOe. The saturation magnetization values were determined from the hysteresis loops. Additional magnetic force microscopy (MFM) measurements were performed using Asylum Research Atomic Force Microscope to map the magnetic field distribution of FeMn-3Ag and FeMn-5Ag samples. MFM measurements were performed in two pass mode; in the first pass topography of the sample surface was obtained, while in the second pass magnetic forces between previously magnetized tip and the sample were sensed at the lift height of 30 nm. All the measurements were performed at remanence state of the as-grown samples.

2.2. Computational details

In this work, the Vienna *ab initio* simulation package (VASP) density functional theory (DFT) based on the projector augmented wave method formulated to treat collinear and noncollinear magnetic structures is applied [35–37]. The exchange correlation effect is tuned with the generalized gradient approximation (GGA) by Perdew-Burke-Enzerhof (PBE) [38]. A minimal basis set is adopted, which includes *3d*, *4 s* and *4p* orbitals having a cutoff of 300 eV.

The ordered γ-FeMn austenite is treated using the primitive CuAu-I-unit cell [37,39] and a 2 × 2 × 2 supercell using (4 × 4 × 4) and (8 × 8 × 8) k-points meshed to sample the Brillouin zone. The antiferromagnetic (AFM) spin configurations are notated by 1Q (collinear) and 2Q or 3Q (non-collinear) including several Fe and Mn moments directions in line with previous reports [35,39]. In particular, in 1Q there are several combinations of the atomic moments' alignment in the unit cell *e.g.*, antiparallel Fe-Fe (↑↓) and Mn-Mn (↑↓) moments or parallel Fe-Fe (↑↑) and Mn-Mn (↓↓) moments [35]. In 2Q the moments in the four-atom CuAu-I unit cell can be along [$\bar{1}$00], [100], [0$\bar{1}$0], [010] or along [110], [$\bar{1}\bar{1}$0], [1$\bar{1}$0], [$\bar{1}$10] *etc.* while in 3Q spins can point to the cell center or have any directions in the three axes [35,39]. In addition, in *ab initio* calculations the atomic percent is used, therefore γ-FeMn represents the γ-Fe$_{50}$Mn$_{50}$ (at%) or γ-Fe$_{49.59}$Mn$_{50.41}$ (wt%) in atomic or weight percent, respectively. The calculations started at the experimental lattice constant of γ-FeMn at zero temperature (a = 3.60 Å) choosing the same spin states with the available theoretical data [37, 39–41] for comparison reasons while cell and atomic relaxation were also employed in several ordered, disordered and Fe- or Mn- rich first neighborhood Ag environments having 16 or 32 atoms, offering in total 58 different configurations. In particular, in the 32 atoms supercell, 1 Fe was replaced by Ag in order to mimic the different Fe-Mn neighborhoods of Ag resulting in system of γ-Fe$_{46.875}$Mn$_{50}$Ag$_{3.125}$ (at%) or γ-Fe$_{45.91}$Mn$_{48.18}$Ag$_{5.91}$ (wt%) having 15 Fe, 16 Mn and 1 Ag atoms. When replacing 1 Mn, the γ-Fe$_{50}$Mn$_{46.875}$Ag$_{3.125}$ (at%) or γ-Fe$_{48.915}$Mn$_{45.14}$Ag$_{5.91}$ (wt%) crystal have 16 Fe, 15 Mn and 1 Ag atoms. Moreover, the cases of replacing 1 Fe and 1 Mn atoms by Ag atoms were considered, in order to mimic the cases with Ag first neighbors, resulting in γ-Fe$_{46.875}$Mn$_{46.875}$Ag$_{6.25}$ (at%) or γ-Fe$_{44.62}$Mn$_{43.89}$Ag$_{11.49}$ (wt%). It should be noted that although the theoretical atomic percentages are not exactly the ones of the experimental weight percentages, they offer a good description of the behaviour of γ-FeMn upon Ag addition. The *ab initio* calculations were performed at FeMn-6Ag (wt%) which is close to FeMn-5Ag (wt%), where the experiments already revealed the appearance of the martensite phase and a slight increase of magnetization. The higher Ag content of γ-Fe$_{44.62}$Mn$_{43.89}$Ag$_{11.49}$ (wt%), named FeMn-12Ag (wt%), was also considered to study the cases of having two Ag as first neighbors and to investigate the trends of the structural and magnetic properties upon further increase of the Ag percentage.

Similarly, the ε-FeMn martensite primitive unit cell and 16 or 32 atoms' supercells were used along with a (8 × 8 × 8) k-point mesh in the suggested collinear AFM spin state having pure Fe or Mn atomic [0001] layers (named herein pure[0001]) [42] and a system with mix Fe-Mn [0001] layers, as expected due to the geometry of ordered γ-FeMn (111) austenite structure, resulting in 26 configurations (named herein FeMn [0001]). In addition, ε-FeMn represents the ε-Fe$_{50}$Mn$_{50}$ (at%) and ε-Fe$_{49.59}$Mn$_{50.41}$ (wt%) in atomic and weight percent, respectively. The Ag substitution in ε-FeMn was accounted in a similar way as for γ-FeMn, resulting in ε-Fe$_{45.91}$Mn$_{48.18}$Ag$_{5.91}$ (wt%) or ε-Fe$_{48.915}$Mn$_{45.14}$Ag$_{5.91}$ (wt %) for the different first neighbor environments (when replacing Fe or Mn by Ag) named therefore ε-FeMn-6Ag. The case of both Fe and Mn atoms' substitution results in ε-Fe$_{44.62}$Mn$_{43.89}$Ag$_{11.49}$ (wt%) and named ε-FeMn-12Ag in wt% for an easier comparison with the experimental data.

The atomic relaxations were continued until the Helmann-Feynman forces acting on the atoms were less than 0.01 eV/Å and the total energy changes were less than 10^{-6} eV. All the calculations were carried out in spin-polarized mode.

3. Results and discussion

3.1. Effect of Ag addition on microstructure of FeMn alloys

The SEM images of the synthesised porous alloys are shown in Supplementary Fig. S1. The alloys show a similar porous microstructure, with macropores of around 20 μm for all the investigated compositions. The percentage of macroporosity, calculated from the SEM images, was between 18% and 22% and increased slightly with Ag content. Fig. 1 shows the XRD patterns of the four studied alloys. Equiatomic FeMn and FeMn-1Ag samples mainly possess the face-centered cubic (fcc) γ-austenite phase, which is in accordance with the Fe-Mn phase diagram for this composition [43]. Meanwhile, the FeMn-3Ag and FeMn-5Ag samples consist of a mixture of phases, namely fcc γ-austenite and hexagonal close-packed (hcp) ε-martensite phases. This is a rather surprising result given the small amount of added Ag. In fact, the martensitic phase in FeMn alloys is typical for lower Mn contents, of 15 −30 wt% [18,44]. It has been reported that the driving force for the ε-martensite phase is the low stacking fault energy upon the addition of manganese and other elements to Fe [8]. Our results reveal that the addition of small amounts of Ag may significantly contribute to the γ to ε phase transformation. Fig. 1 also reveals small amounts of iron-manganese oxides formed during the sintering process. The weight percentage of phases was calculated using X′Pert HighScore Plus software and the results have shown that the percentage of martensite content increases from 0 wt% in FeMn to 71.5% and 77 wt% in FeMn-3Ag and FeMn-5Ag, respectively. Accordingly, the percentage of austenite decreases from 100% in FeMn to 26.5% and 23 wt% for FeMn-3Ag and FeMn-5Ag, respectively.

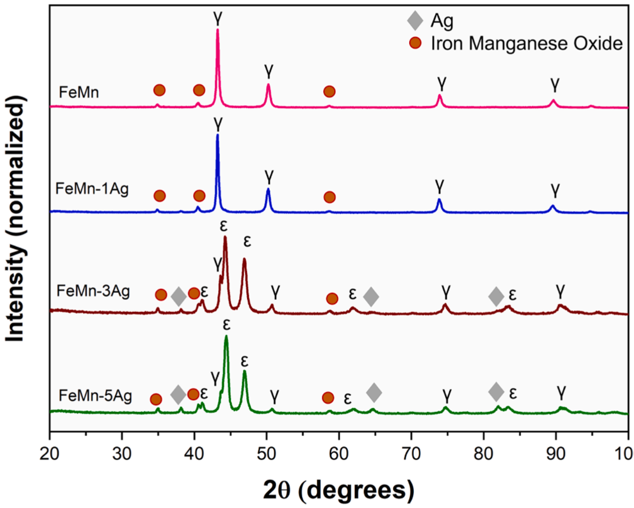

Fig. 1. XRD patterns of FeMn, FeMn-1Ag, FeMn-3Ag and FeMn-5Ag sintered alloys. The symbol γ corresponds to fcc austenite, while ε denotes the peaks from hcp martensite phase.

Figs. 2 and 3 show the bright-field TEM images of the FeMn and FeMn-5Ag samples, respectively, together with their selected area electron diffraction (SAED) patterns. The samples were cut from a dense area to avoid the occurrence of pores. These figures clearly demonstrate the distinct features of the two samples. In Fig. 2(a,b), the FeMn alloy (with no Ag) shows the presence of elongated grains, with a thickness of approximately 20 nm. The microstructure contains a large number of defects, and it is difficult to clearly define the grain boundaries. The SAED pattern, shown in Fig. 2(c), confirms the presence of γ-austenite, where (111), (200), (220) and (311) planes were identified, with a lattice constant of 3.56 ± 0.03 Å. This value is in accordance with the lattice constant of the γ-austenite phase in Fe-40Mn alloy as described in the literature [45]. In Fig. 2(a) we can observe some bright, rounded particles, with a diameter of approximately 200 nm, which can be attributed to iron-manganese oxide, as also detected in the corresponding XRD pattern (Fig. 1).

In the FeMn-5Ag sample presented in Fig. 3, the grains are more equiaxed and larger, with a size of approximately 400 nm. The grain boundaries are very well defined. Apart from austenitic grains, the ε phase is also present, as shown in Fig. 3(a) (orange) and confirmed by SAED (Fig. 3b). Specifically, the reflections from $(111)_\gamma$, $(200)_\gamma$ and $(100)_\varepsilon$ were identified in Fig. 3(b). Meanwhile, spots attributed to γ austenite are present in Fig. 3(c). The lattice constant of the γ phase was 3.56 ± 0.04 Å. The a lattice constant of the ε martensite, calculated based on the (100) interplanar distance, was 2.53 ± 0.03 Å, which agrees with values reported in literature [46]. The high-resolution image in Fig. 3d together with the FFT analysis performed in the region

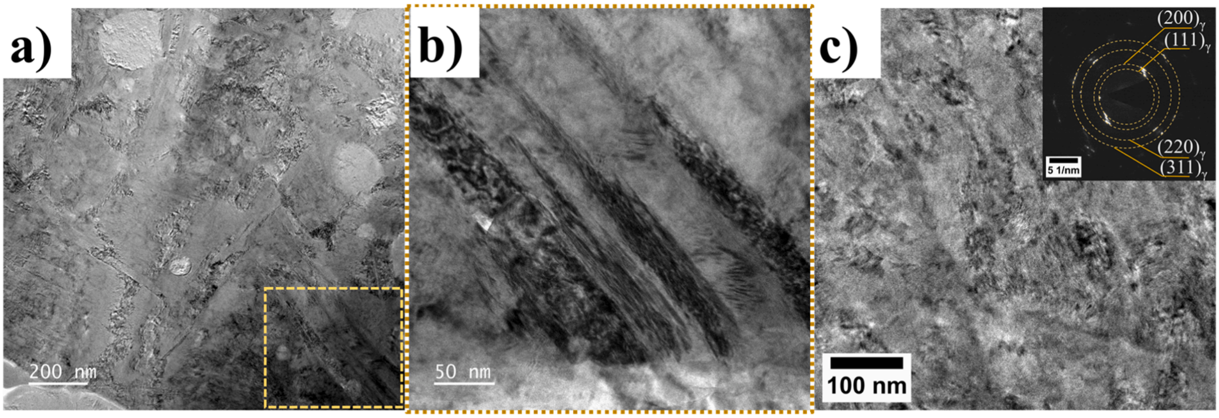

Fig. 2. TEM images of FeMn alloy: (a) low magnification image, (b) magnified detail of the area enclosed within the yellow square in panel a), (c) STEM image together with SAED pattern.

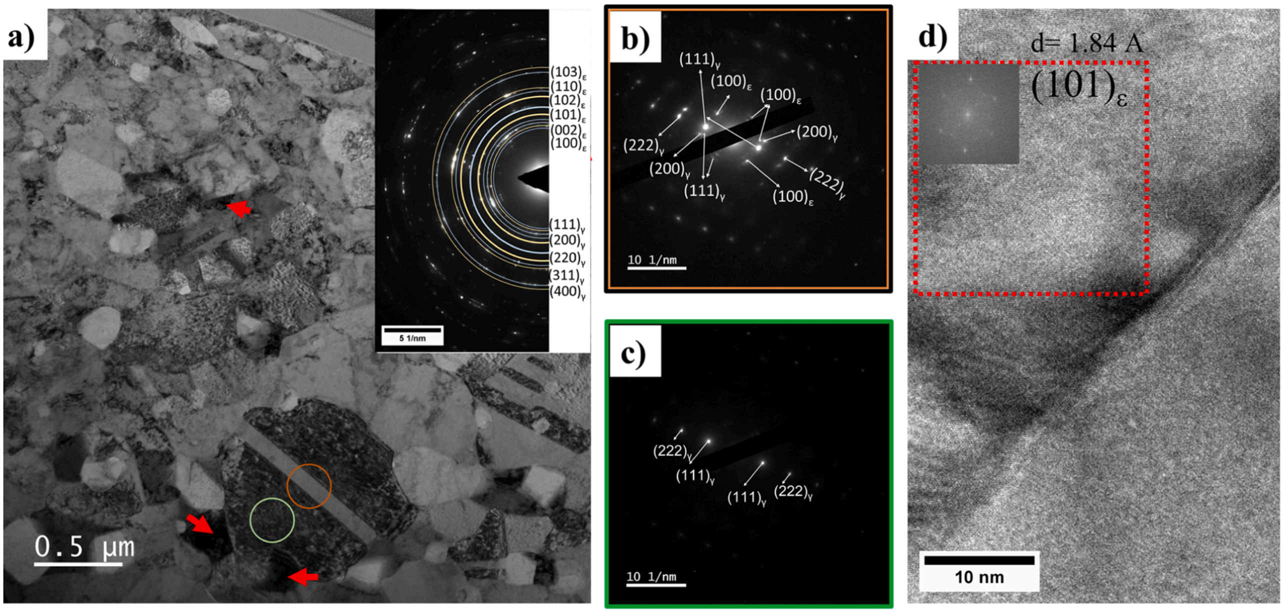

Fig. 3. TEM images of FeMn-5Ag alloy (a) low magnification image with red arrows pointing to Ag particles. The inset shows the corresponding, indexed SAED pattern where blue lines correspond to ε phase and yellow lines to γ phase. (b) SAED pattern of the region enclosed in the orange circle in panel a) and (c) SAED pattern of the region enclosed in the green circle in panel a), (d) high-resolution STEM image with the FFT performed on the highlighted area in red, indicating the occurrence of ε phase.

highlighted in red shows the presence of the ε-martensite (101) plane. Moreover, apart from the austenite and martensite phases, Ag-rich particles were identified and highlighted in Fig. 3(a) with red arrows and confirmed by high-angle annular dark field (HAADF) and EDS analysis, presented in Supplementary Fig. S2. These particles had a diameter of 150–300 nm. As expected, Ag is lowly soluble in the FeMn matrix, and therefore Ag precipitates also form.

A similar morphology of the ε phase has been observed in the literature [47–49]. This platelet structure of ε martensite, as shown in Fig. 3 (a), subdivides γ grains by moving from one-grain boundary to the other on the opposite side, which was identified as Type II ε-martensite [49]. The subdivision of γ grains leads to a dynamic grain refinement, which in turn may lead to an improvement in the mechanical properties of the Ag-containing alloys. The type of martensite formed depends on the initial size of the γ grains and it has been shown that an extensive grain refinement suppresses the γ to ε transformation [49]. This may be the reason why the martensite phase is observed only in the big grains of the γ phase.

3.2. *Effect of Ag on atomic structure and spin configurations*

Aiming to understand the influence of Ag in the structural properties of FeMn-Ag alloys, DFT calculations were performed for several atomic rearrangements in γ-FeMn and ε-FeMn and spin states. The starting points were the AFM collinear (1Q) and non-collinear (2Q or 3Q) spin states for the γ-FeMn primitive unit cell available in the literature [37,39,42] along with the AFM collinear ε-FeMn phases [42], as shown in Fig. 4(a,b). These DFT studies on γ-FeMn alloys with collinear or non-collinear spin states found for the γ-$Fe_{50}Mn_{50}$ an energy preference towards the 2Q and 3Q states along with an underestimation of the experimental lattice constant (3.54 Å with GGA and 3.42 Å with local density approximation (LDA) [37,39,42]) except from the introduced frozen core approximation in the exact muffin-tin orbital (EMTO-DFT) method [39]. To this end, most of the previous theoretical studies on γ-$Fe_{50}Mn_{50}$ were performed at the experimental lattice constant (3.63 Å) or its extrapolation at zero temperature (3.60 Å) [37,39] since it was really interesting to understand the existence of different AFM (1Q, 2Q, 3Q) spin states and verify the related lack of experimental

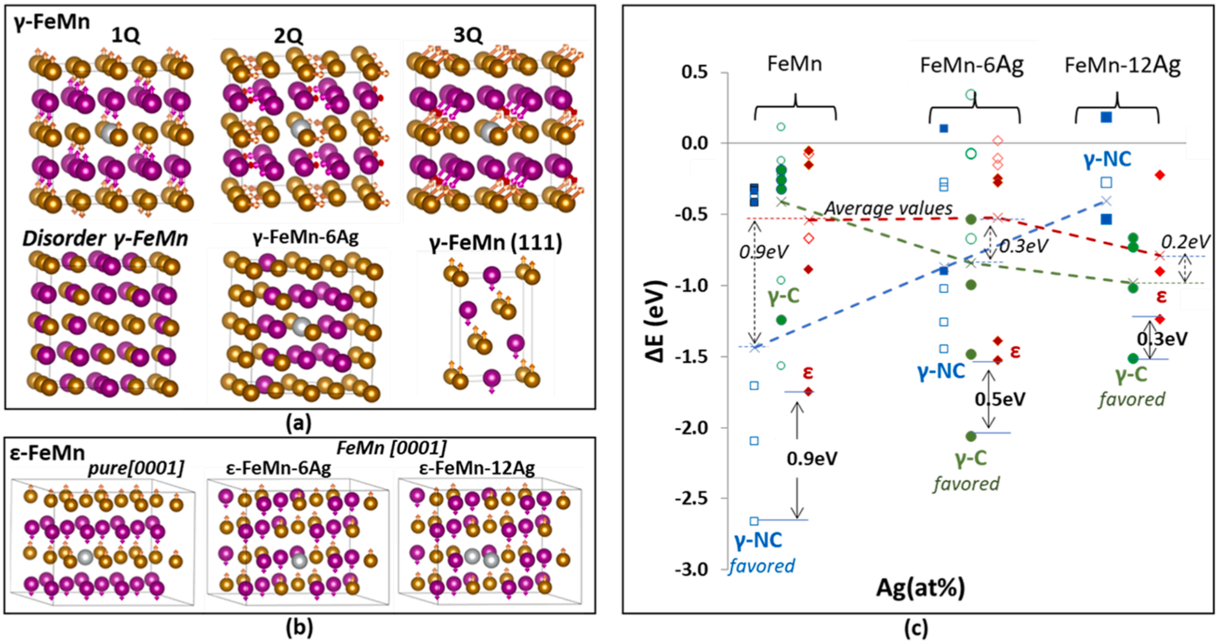

Fig. 4. FeMn-Ag alloys' selective atomic structures for (a) austenite and (b) martensite phases along with the main AFM collinear (1Q) and non-collinear (2Q and 3Q) spin states. Fe, Mn and Ag atoms are depicted by gold, magenta and grey spheres. (c) Total energy difference ΔE of AFM collinear and non collinear spin states for different atomic rearrangements and crystal structures. ΔE's negative values denote alloy stability against their corresponding pure element phases. Open and filled symbols represent the DFT results on the theoretical and the experimental lattice constants while γ-Collinear (γ-C in green circles), γ-Non-Collinear (γ-NC in blue squares) and ε-Collinear (ε in red diamonds) stand for spin states. As a guide to the eye, dashed lines correspond to the average ΔE values of all under-study stable ($\Delta E < 0$) configurations for each structure γ-C (green line), γ-NC (blue line) and ε (red line) that might coexist in the experimental conditions. The difference between the γ and ε phases' energetically favoured ΔE values is denoted by a black vertical arrow while the corresponding deviation between the average values is shown with dashed vertical arrows. The compositions FeMn-6Ag (wt%) describe the γ-$Fe_{45.91}Mn_{48.18}Ag_{5.91}$ (wt%) and γ-$Fe_{48.915}Mn_{45.14}Ag_{5.91}$ (wt%) cases while FeMn-12Ag (wt %) refers to $Fe_{45.75}Mn_{46.51}Ag_{11.49}$ (wt%).

consensus concerning the favoured spin configurations. In line with these previous calculations, the current DFT results also underestimate the γ-FeMn lattice constant (3.53 Å and 3.54 Å for the collinear and non-collinear primitive unit cells) compared with the projected augmented wave (PAW) method (3.53 Å) and simple EMTO (3.54 Å) [39] and the experimental results of this work, presented in Fig. 1. Therefore, in Fig. 4(c) the current DFT results are presented for both cases: i) at the experimental lattice constant (filled symbols) and ii) for the totally relaxed (unit cell and atomic positions) configurations (open symbols). The total energy difference (ΔE) was estimated for all cases using the $E_{FeMn\text{-}Ag}$ total energy corresponding to all studied spin states, compositions and atomic environments in order to reveal the energetically favoured structure using the expression (Eq. 1):

$$\Delta E = E_{FeMnAg} - (N_{Fe}E_{Fe} + N_{Mn}E_{Mn} + N_{Ag}E_{Ag}) \qquad (1)$$

where E_{Fe}, E_{Mn} and E_{Ag} stand for the corresponding austenite or martensite single elements' structure and N_{Fe}, N_{Mn} and N_{Ag} are the related number of atoms. ΔE was calculated in order to be able to compare different phases, Ag contents and cells' sizes. It should be noted that although several units and supercells (ordered or even disorder-like) are chosen in this work, in total 84 configurations, they cannot be directly compared to the experimentally observed solid solution austenite and martensite phases, which sometimes even co-exist. Nevertheless, they might provide an estimation of the FeMn behaviour upon Ag addition.

Starting with the binary alloy, for the γ-FeMn collinear states (1Q) different AFM spin moment combinations on the 4-unit cell's atoms (up or down) have been considered following the spin configurations depicted in [37] and presented in Fig. 4(c) with filled green spheres. Although the energy difference between the several collinear AFM spin states is small (up to 0.05 eV/atom) in line with [37], the results of this work reveal the AFM collinear 1Q of Fig. 4(a) that has antiparallel Fe-Fe (↑↓) and Mn-Mn(↑↓) moments as the most energetically favored [37,39]. Nevertheless, the non-collinear 2Q (having the spins pointing along the [110], $[\bar{1}\bar{1}0]$, $[1\bar{1}0]$, $[\bar{1}10]$ as in [39]) and 3Q (with spins towards the center of the unit cell, similar to [35,39]) are energetically favored against all collinear configurations, in line with previous studies [37, 39]. It should be noted that the non-collinear energetically favored γ-FeMn of this work has the Fe moments parallel to each other and the Mn moments creating a global anti-parallel magnetization as expected from the approach we have used [37]. The γ-FeMn disorder relaxed supercell also shows a preference towards the non-collinear state (−2.09 eV) compared to the collinear state (−0.96 eV) while the collinear γ-FeMn unit cell of the (111) face (−0.22 eV) has almost the same energy with all collinear γ-FeMn primitive unit cells (oriented along (001)) as expected. Concerning the martensite ε-FeMn, the experimentally suggested structure having pure [0001] Fe or Mn atomic layer sequence [42] was considered and found to be unfavored (−0.88 eV) compared to mixed FeMn [0001] atomic layers which are related to the γ-FeMn (111) face geometry (−1.75 eV), both calculated at the experimental lattice constants $a = 2.53$ Å and $c = 4.079$ Å of ε-$Fe_{80}Mn_{20}$ [50], Fig. 4(b). Similar ε-FeMn mixed structure preference was found when using the present work's ε-$Fe_{50}Mn_{50}$ lattice constants $a = 2.47$ Å and $c = 3.93$ Å having only a ΔE underestimation (the FeMn [0001] shows −0.66 eV against pure [0001] ε-FeMn −0.07 eV). It should be noted that the AFM collinear and non-collinear ε-FeMn states reveal equivalent ΔE (the difference might be 0.01 eV) and therefore are presented in Fig. 4(c) with the same symbol (diamond).

Turning on the ternary FeMn-Ag system, the same austenite and martensite binary supercells were used to reveal the effect of Ag substitution, as shown in Fig. 4(a,b). In the ordered γ-FeMn-6Ag (wt%), the two available cases of Fe (γ-$Fe_{46.875}Mn_{50}Ag_{3.125}$ (at%) or γ-$Fe_{45.91}Mn_{48.18}Ag_{5.91}$ (wt%)) or Mn (γ-$Fe_{50}Mn_{46.875}Ag_{3.125}$ (at%) or γ-$Fe_{48.915}Mn_{45.14}Ag_{5.91}$ (wt%)) substitution by Ag atoms were considered. In Fig. 4

(a), the energetically favored γ-FeMn-6Ag (γ-$Fe_{46.875}Mn_{50}Ag_{3.125}$ (at%) or γ-$Fe_{45.91}Mn_{48.18}Ag_{5.91}$ (wt%)) atomic and spin configurations are presented where Ag prefers to have as many as possible Mn atoms in the first neighborhood. In particular, the collinear 1Q AFM γ-$Fe_{45.91}Mn_{48.18}Ag_{5.91}$ (wt%) (−2.06 eV) of Fig. 4(a) is favored against the collinear 1Q AFM γ-$Fe_{48.915}Mn_{45.14}Ag_{5.91}$ (wt%) (−1.48 eV) with more Fe atoms as seen in Fig. 4(b). Interestingly, all γ-FeMn-6Ag (wt%) non-collinear states are less preferred compared to the binary FeMn cases while the average ΔE (dashed lines) shows equivalent values between γ-NC and γ-C. Furthermore, Ag prefers the FeMn [0001] martensite ε-FeMn-6Ag (wt%) configuration by 1 eV against the pure [0001] as well as the Fe atomic position (−1.53 eV in Fe site, ε-$Fe_{45.91}Mn_{48.18}Ag_{5.91}$ (wt%), and − 1.39 eV in Mn site, ε-$Fe_{48.915}Mn_{45.14}Ag_{5.91}$ (wt%). Fig. 4(c)). Similar preference was observed for the austenite phase, revealing the Ag preference towards a ‘rich in Mn’ 1st neighborhood environment.

Upon Ag enrichment, in $Fe_{45.75}Mn_{46.51}Ag_{11.49}$ (wt%) or FeMn-12Ag (wt%), where two Ag atoms might become first neighbours, the austenite collinear states are favored compared to the non-collinear ones while including the martensite cases all ΔE values decrease, as shown in Fig. 4(c). Moreover, at much higher Ag compositions, *e.g.* the FeMn-39Ag (wt%) which describes the four atom primitive γ and ε unit cells with compositions γ-$Fe_{40.16}Mn_{20.41}Ag_{39.43}$ (wt%) and γ-$Fe_{20.01}Mn_{40.69}Ag_{39.30}$ (wt%) (not included in this figure), the ΔE values become positive revealing this system's instability. Concerning the spin states, the γ-$Fe_{45.75}Mn_{46.51}Ag_{11.49}$ (wt%) or γ-FeMn-12Ag (wt%) AFM 1Q (−1.51 eV) state and the ε- $Fe_{45.75}Mn_{46.51}Ag_{11.49}$ (wt%) or ε-FeMn-12Ag (wt%) in the mix FeMn [0001] (−1.23 eV) configuration seem to be the preferred ones (Fig. 4(b, c)).

Overall, the results shown in Fig. 4(c) indicate that the energy difference between the austenite and martensite phase progressively decreases with the increase of Ag content as denoted by continuous black vertical arrows in Fig. 4(c) between the energetically favored structures or with a dashed black vertical arrow between the average ΔE values of all stable understudy (dashed blue, green and red lines stand for γ-NC, γ-C and ε configurations). In particular, for FeMn the energy difference between the favored γ-NC (ΔE = −2.66 eV) and ε (ΔE = −1.75 eV) is 0.9 eV, while for γ-$Fe_{45.91}Mn_{48.18}Ag_{5.91}$ (wt%) or γ-FeMn-6Ag (wt%) the γ-C (ΔE = −2.06 eV) becomes favored against γ-NC and differs to ε (ΔE = −1.53 eV) by 0.5 eV and is further reduced to 0.3 eV at $Fe_{45.75}Mn_{46.51}Ag_{11.49}$ (wt%) or FeMn-12Ag (wt%). Similarly, the difference between the average ΔE austenite and martensite values decreases from 0.9 eV (FeMn, γ-NC and ε) to 0.3 eV ($Fe_{45.91}Mn_{48.18}Ag_{5.91}$ (wt%) or FeMn-6Ag(wt%), γ-C and ε) and 0.2 eV ($Fe_{45.75}Mn_{46.51}Ag_{11.49}$ (wt%) or FeMn-12Ag(wt%), γ-C and ε). The small energy difference (0.3 eV on average or 0.5 eV in favoured cases) between these austenite and martensite states in $Fe_{45.91}Mn_{48.18}Ag_{5.91}$ (wt%) or FeMn-6Ag(wt%) explains the experimental results of this work, which found a co-existence of both phases at FeMn-5 wt% Ag (Fig. 1).

3.3. *Intrinsic stacking fault energy considerations*

Aiming to further understand the influence of Ag addition on the FeMn austenite-to-martensite phase transformation, the intrinsic stacking fault energy was evaluated. The pure Fe and FeMn cases were considered first due to the absence of FeMn-xAg stacking fault energy calculations. Concerning the non-magnetic pure Fe at 0 K, previous *ab initio* calculations revealed that the hexagonal close packed stacking is energetically favored with respect to the fcc stacking [13–15]. Therefore, the fcc(111) structure with an intrinsic stacking fault plane (…ABCABCA|CABC…) that locally mimics the hcp stacking plane is more stable than the perfect fcc phase [13–15]. It should be noted that in the fcc phase there might be several stacking faults irregularities in the three ABC (111) atomic planes' sequence. The perfect ABCABCABC stacking sequence could change to: a) twin boundary that has a twin mirror plane ABC$\underline{\mathrm{A}}$CBA, b) the intrinsic stacking fault (ISF) that has a "missing" plane due to shear and a sequence ABCABCA|CABC while c) the extrinsic stacking fault ABCA$\underline{\mathrm{C}}$BABC that has an extra plane. This description becomes more complicated in the case of alloys like γ-TiAl or γ-FeMn where the local chemical neighborhood or magnetism are also involved. In this work the intrinsic stacking fault was considered since it is directly related to the generalized stacking fault energy or γ surface that is defined by shearing two parts of the crystal with respect to each other along a certain plane (here in the (111) plane). The intrinsic stacking fault corresponds to a particular shear point ($\vec{u}/3$ along the $[1\bar{2}1]$) where the existence of a minimum on the γ surface suggests that the transition is favoured [13,14,51–53].

The pure Fe and FeMn supercells having 6 fcc(111) unit cells along the [111] axis and periodic boundary conditions in the in-plane meshed by 2 × 4 × 1 k-points were firstly considered following Bleskov [13] and Gholizadeh et al. [14]. In Fig. 5(a) the case of FeMn is presented in the perfect austenite γ-phase (oriented along fcc(111) having the stacking sequence of ABCABC) as well as the ISF which stands for shear of the γ-phase by $\vec{u}/3$ along the $[1\bar{2}1]$ resulting the intrinsic stacking fault plane (…ABCABCA|CABC…) presented with a dashed black line. In Fig. 5(a) the γ-FeMn 36 atoms' supercell represents the γ-$Fe_{50}Mn_{50}$ (at %) or γ-$Fe_{49.59}Mn_{50.41}$ (wt%) in atomic or weight percent, respectively while in (b) the refers to γ-$Fe_{47.2}Mn_{50}Ag_{2.77}$ (at%) or γ-$Fe_{46.41}Mn_{48.34}Ag_{5.26}$ (wt%) having 17 Fe, 18 Mn and 1 Ag atoms named for simplicity FeMn-5Ag and in (c) the γ-$Fe_{47.22}Mn_{47.22}Ag_{5.55}$ (at%) or γ-$Fe_{45.23}Mn_{44.50}Ag_{10.27}$ (wt%) having 17 Fe, 17 Mn and 2 Ag atoms named for simplicity FeMn-10Ag. In Fig. 5(b,c) the FeMn-Ag cases were named FeMn-5Ag (wt%) FeMn-10Ag (wt%) for easier comparison with our experimental data.

The intrinsic stacking fault energy (γ_{ISF}) excess due to the defect formation is given by Eq. (3):

$$\gamma_{ISF} = (G_{def} - G_{ideal})/S \tag{3}$$

where G_{def} is the energy of the supercell with defects (the ε-like phase herein), G_{ideal} is the energy of the ideal fcc(111) (the γ- phase herein) and S is the interface area over which the defect is extended [13,14]. The γ_{ISF} of non-magnetic Fe, − 424 mJ m^{-2} for the optimized 3.45 Å lattice constant, is in line with the previous reports on *ab initio* calculations for this material, *i.e.*, − 422 mJ m^{-2} and − 451 mJ m^{-2} [13], − 464 mJ m^{-2} [15] and − 450 mJ m^{-2} [14].

Similar ISF values were predicted for FeMn (−501 mJ m^{-2}), as shown in Fig. 5(a), compared to non-magnetic disordered fcc Fe-Mn 22.5 at% (−450 mJ m^{-2}) alloys and paramagnetic Fe-Mn40at% (−325 mJ m^{-2}) [51] as well as − 510 mJ m^{-2} for $Fe_{23}Mn_1$ [52]. It should be noted that although the *ab initio* values are really far from the experimental values of 15–33 mJ m^{-2} for Fe-Mn alloys [53] due to the tiny and perfect (using periodic boundary conditions) supercell, they already reveal that the ISF structure is favored over the ideal fcc perfect structure.

The next step was to substitute Fe or Mn atoms by Ag starting from the Fe position since Ag prefers the Mn first neighbor atoms, as described in Section 3.2 and observed in Fig. 4.

In Fig. 5(b) the $Fe_{46.41}Mn_{48.34}Ag_{5.26}$ (wt%) or FeMn-5Ag (wt%) case is presented in two atomic AFM configurations having the Ag atom in the stacking fault plane (ΔE = −0.87 eV) in a Fe position that is less favored compared to a possible Fe (ΔE = −1.04 eV, $Fe_{46.41}Mn_{48.34}Ag_{5.26}$ (wt%)) or Mn (ΔE = −1.13 eV, $Fe_{49.11}Mn_{47.22}Ag_{5.26}$ (wt%)) site further from the stacking fault plane. These results suggest that atomic Ag could exist in several positions (close or not to the stacking fault plane) since the difference in ΔE between different sites is 0.1–0.2 eV. Similar energies are expected in lower Ag compositions, like FeMn-1Ag (wt%) and FeMn-3Ag (wt%), where the probability of Ag atoms having Fe and Mn neighbor atoms is enhanced compared to Ag-Ag first neighbors.

Nevertheless, using the present supercells, higher Ag compositions

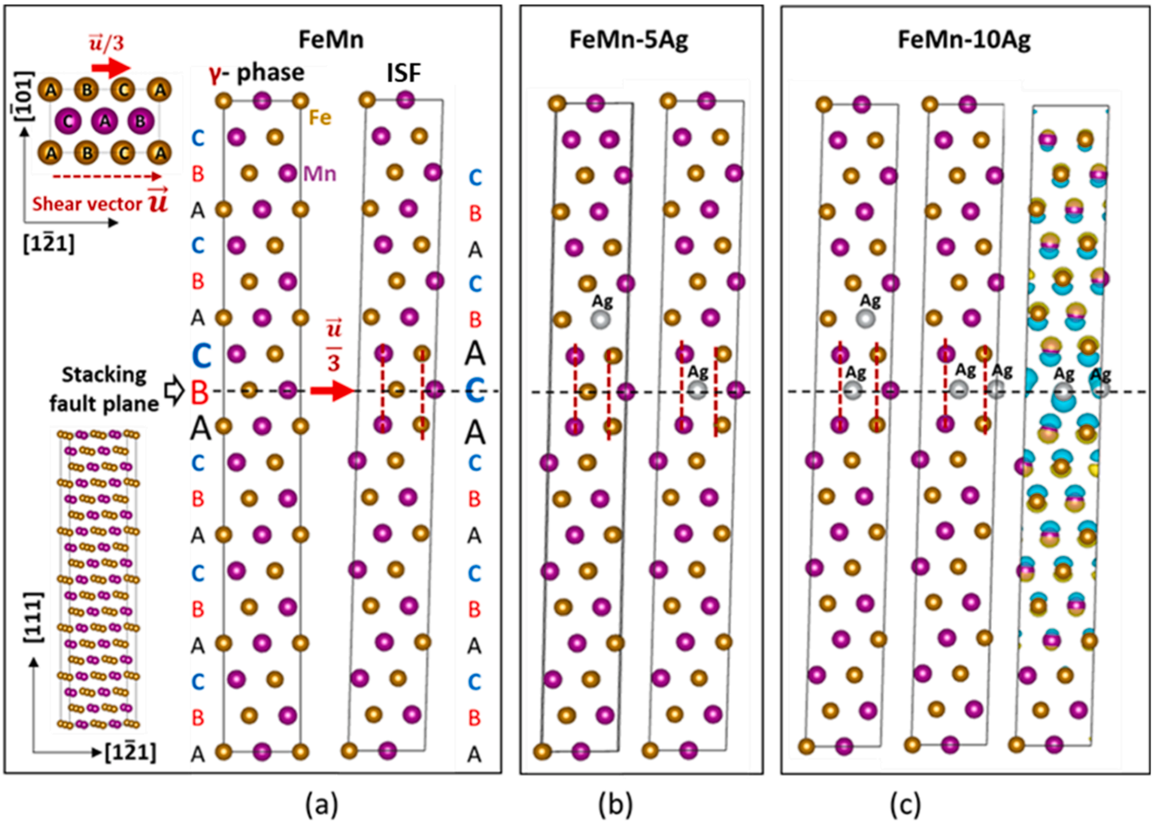

Fig. 5. FeMn-xAg(111), x = 0, 5, 10 wt% atomic representation of the intrinsic stacking fault structures for characteristic cases. Fe, Mn and Ag atoms are presented by gold, magenta and grey spheres. Dashed line denotes the stacking fault plane. The compositions FeMn-5Ag (wt%) describe the $Fe_{46.41}Mn_{48.34}Ag_{5.26}$ (wt%) and $Fe_{49.11}Mn_{47.22}Ag_{5.26}$ (wt%) cases while FeMn-10Ag (wt%) refers to $Fe_{45.23}Mn_{44.50}Ag_{10.27}$ (wt%). In Fig. 5(c) the electron charge density difference is also plotted along with atoms where the light blue semicircles denotes depletion of the electron charge that is enhanced close to the stacking plane.

can be achieved where two Ag atoms might be first, second or third neighbors. In Fig. 5(c) for $Fe_{45.23}Mn_{44.50}Ag_{10.27}$ (wt%) or FeMn-10Ag (wt%) the cases of Ag-Ag atoms being third ($\Delta E = +0.04$ eV) neighbors (one Ag atom is at the stacking plane and another one two layers further) is unstable while the case where both Ag atoms are neighbors and fully occupy the stacking fault plane ($\Delta E = -1.22$ eV) is favored occupying. The FeMn-10Ag (wt%) where both Ag atoms are first neighbors but lay two atomic layers further from the stacking fault plane ($\Delta E = -0.45$ eV) is less favored. Nevertheless, the preference of having in the system Ag-Ag first neighbors with stable configuration ($\Delta E < 0$) is in line with the existence of Ag particles in FeMn-5Ag(wt%) (see Fig. 4). Although, there are several atomic configurations and rearrangements that someone could take into account, the ones presented in Fig. 5(b,c) and described in this paragraph are characteristics and could interpret the Ag behaviour close to the stacking fault plane.

The FeMn-5Ag(wt%) intrinsic stacking fault energies with Ag atom occupying a Fe site at the SF plane (ISF = -424 mJ m^{-2}) or two layers further from it (ISF = -457 mJ m^{-2}) increase compared to FeMn (ISF -501 mJ m^{-2}) but remain negative denoting the possible existence of both phases in the crystal.

Upon full occupation of the stacking fault plane by Ag in FeMn-10Ag (wt%) ISF decreases to ISF $-$ 440 mJ m^{-2} while a smaller reduction is found for the partial Ag occupation of the stacking plane ISF = -413 mJ m^{-2}, thus showing the tendency of the system towards the martensite structure in both configurations. In Fig. 5(c), the electron charge density difference is presented where depletion of the electron charge (light blue area) close to the stacking plane and the nearest neighboring atomic layers thus weakening the interatomic bonds and allowing therefore an easier slip of atoms and therefore a phase transition from the austenite towards martensite structure.

3.4. *Effect of Ag on mechanical and magnetic properties of FeMn alloys*

The mechanical and magnetic properties of the samples under study were experimentally determined to assess the impact of the Ag content on these properties. The compressive stress-strain curves of the studied FeMn-xAg samples are presented in Fig. 6. The average values of the compressive yield strength ($R_{0.2}$), compressive ultimate strength (R_m)

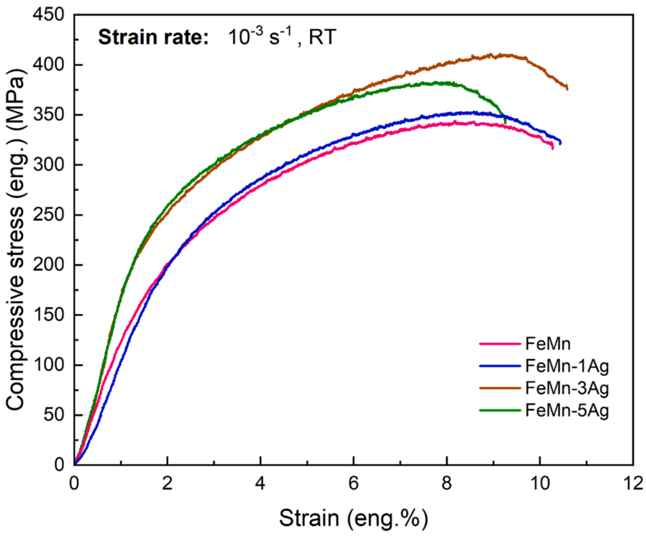

Fig. 6. Compression stress-strain curves for FeMn, FeMn-1Ag, FeMn-3Ag and FeMn-5Ag samples. Tests were performed at a strain rate of 10^{-3} s^{-1} and halted at fracture.

and compressive strain (*A*) are presented in Table 1. The shape of the curves indicates the high ductility of the sample, especially considering its high porosity. All tested samples possess a high 0.2% compressive offset yield strength ($R_{0.2}$), above 181 MPa. Among all tested samples, FeMn-3Ag and FeMn-5Ag show the highest compressive strength (430 and 398 MPa, respectively) compared to FeMn and FeMn-1Ag, as presented in Fig. 6. The highest values of $R_{0.2}$ were obtained for the FeMn-5Ag sample (254 MPa), whereas FeMn-3Ag possesses the highest compressive strength (430 MPa).

FeMn-5Ag and FeMn-3Ag alloys exhibit better mechanical properties at compression than FeMn and FeMn-1Ag alloys, with the maximum 40% increase in $R_{0.2}$ and 28% increase in R_m. This increase in mechanical strength is mainly attributed to the different phase compositions of the Ag-containing samples as well as to Ag precipitation at the grain boundaries, which leads to precipitation strengthening. The martensite platelets and Ag precipitates act as planar obstacles and can reduce the mean free path of the dislocation movement, thereby strengthening the material [9,54]. A similar increase in the mechanical properties of Ag-containing FeMn alloys was previously observed by Liu et al. [55], where the addition of 0.8 wt% Ag resulted in an increase in yield strength from 94 to 130 MPa, which was mainly attributed to Ag-rich particles on the grain boundaries. Even a small addition of 1 wt% Ag leads to an improvement in the mechanical properties when compared to the FeMn alloy. Moreover, the addition of Ag does not cause changes in the compressive strain and the values oscillate between 7.7% and 8.8%.

In Table 1, the literature values of $R_{0.2}$, R_m and *A* are presented for various porous FeMn alloys. The samples presented in this study show results comparable to the porous, selective-laser-melted (SLM)-fabricated Fe-Mn alloy. At the same time, their strength is higher than that of most other porous alloys formed by sintering of powders. Compared to dense FeMn alloys with similar composition, our materials exhibit lower compression strength because the macropores present in the material act as stress concentration points during deformation.

The magnetic hysteresis loops of the FeMn−xAg alloys, measured by VSM at room temperature, are shown in Fig. 7. The results reveal that the saturation magnetization increases with the Ag content. Among all tested alloys, the highest magnetization value was obtained for the FeMn-5Ag alloy (1.075 emu g^{-1}), whereas the lowest value was obtained for the FeMn alloy without the addition of Ag (0.045 emu g^{-1}). MFM analyses were performed to further study the magnetic behaviour of the samples. The results (see Supplementary Fig. S3) reveal that FeMn-5Ag shows a more pronounced ferromagnetic signal than the FeMn-3Ag sample (for which virtually no magnetic contrast is detected). The magnetic contrast observed for the FeMn-5Ag sample indicates a weakly ferromagnetic response, in agreement with the low saturation magnetization observed in the corresponding hysteresis loop (Fig. 7), which is equivalent to approximately 0.5% the value of M_S of pure Fe ($M_{S,Fe}$ = 220 emu g^{-1}). Since this was a counterintuitive result, DFT simulations were also run, aiming at finding a plausible explanation, as it will be shown below. On the other hand, the fact that M_S is rather low in all investigated material, makes them compatible with MRI scans.

Table 1
Selected parameters calculated from the compression tests: yield strength ($R_{0.2}$), compressive strength (R_m) and compressive strain (A) together with literature values on porous and dense Fe-Mn alloys.

Material	$R_{0.2}$ (MPa)	R_m (MPa)	A [%]	Reference
FeMn	181 ± 6	336 ± 8	8.5 ± 0.50	This study
FeMn-1Ag	205 ± 26	352 ± 14	8.3 ± 0.3	This study
FeMn-3Ag	234 ± 16	430 ± 7	8.8 ± 0.5	This study
FeMn-5Ag	254 ± 10	398 ± 10	7.7 ± 0.3	This study
SLM Fe-35Mn scaffold	89.2 ± 1.9	304.0 ± 7.4	-	[56]
Porous PM Fe-35Mn	64	567	-	[24]
10 wt%HA+Fe30Mn	-	186 ± 12	-	[57]
Porous Fe-44Mn	10 ± 1	-	-	[58]
Dense Fe-30Mn-6Si-1.2Ag	353 ± 34	1849 ± 39	-	[33]

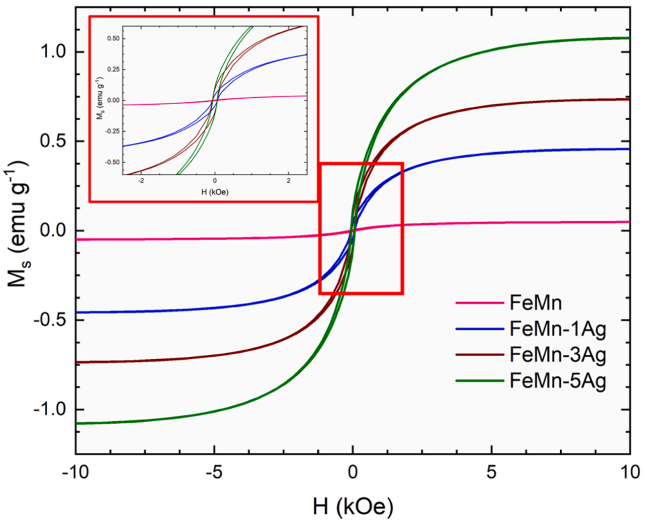

Fig. 7. Magnetization loops of the FeMn, FeMn-1Ag, FeMn-3Ag and FeMn-5Ag samples. Inset shows magnified region between − 2.5 kOe and 2.5 kOe.

3.4.1. *Ag influences the FeMn magnetization and crystal's magnetic moment*

When adding a non-magnetic material like Ag to FeMn, which is well known for its antiferromagnetic properties [59,60], it is not easy to explain the observed increasing magnetization trend of Fig. 7. To this end, the first step is to deeply understand the AFM properties of FeMn. The literature survey reveals many experimental data on Fe_xMn_{1-x} alloys which do not agree on the type of AFM spin states [42,53,59–64]. For example, neutron diffraction experiments found AFM long-range order in chemically disorder bulk γ-$Fe_{0.75}Mn_{0.25}$ [42,59], similar to the 1Q spin state in Fig. 4(a), while Mössbauer neutron diffraction measurements revealed three AFM states depending on the Mn composition named 1Q (the collinear structure for Mn -rich and Fe-rich contents) and 2Q or 3Q (the non-collinear ones for γ-Fe_xMn_{1-x}, $0.3 < x < 0.8$ alloys) [59–61]. Moreover, the addition of Mn drastically reduces the magnetic susceptibility of Fe-based alloys [55] while for Fe_xMn_{1-x}, $0.3 < x < 0.8$ alloys, experiments suggested the 1Q state for $Fe_{0.66}Mn_{0.34}$ [62], the 3Q (partially the 2Q) state for $Fe_{0.5}Mn_{0.5}$ [63] and the 3Q for $Fe_{0.54}Mn_{0.46}$ [64], resulting in a lack of experimental consensus. This behaviour could be attributed to bcc Mn which not only undergoes a first-order transition from a low spin state to high spin state in both ferromagnetic (FM) and AFM states, but it is also sensitive to compression or expansion [65]. To this end, earlier calculations revealed a narrow double moment region where low and high spin states co-exist, giving rise to dissimilar lattice constants [66]. Therefore, the introduction of a third element in the system, like Ag, could introduce local stress (compression or expansion in the interatomic distances) which might lead to different behaviour in the magnetic properties, in line with C addition in Fe-Mn-C, which may give raise to spin-glass-like regions [67]. It is worth reminding here the Ag preference towards Mn's first neighbour atoms as depicted in Fig. 4 (Section 3.2), which means that the electronic and magnetic properties of Mn atoms are mainly affected by Ag atoms. Furthermore, in previous reports describing Fe-30Mn-xAg alloys, the authors found a tendency to decrease the magnetization upon the addition of Ag [30]. For example, in the reports by Liu et al. [30,55], the addition of up to 5 wt% Ag led to a slight decrease in magnetic susceptibility. In our case, the FeMn-xAg, as shown in Fig. 8(a), reveals a small increase in magnetization upon Ag addition which can be a result of the higher Mn amount (~50 wt%) along with the observed phase transformation and the corresponding co-existence of γ and ε phases that

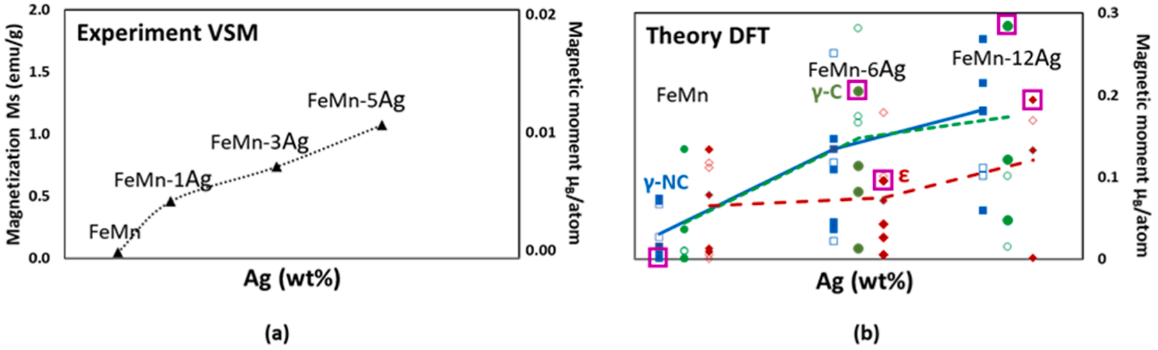

Fig. 8. Magnetization of FeMn-xAg by experimental (a) and theoretical (b) data. In (a) the magnetic moment in μ_B/atom is derived from the Magnetization Ms. The compositions FeMn-6Ag (wt%) describe the γ-$Fe_{45.91}Mn_{48.18}Ag_{5.91}$ (wt%) and γ-$Fe_{48.915}Mn_{45.14}Ag_{5.91}$ (wt%) cases while FeMn-12Ag (wt%) refers to $Fe_{45.75}Mn_{46.51}Ag_{11.49}$ (wt%). In (b) open and filled symbols represent the DFT results on the theoretical and the experimental lattice constants while γ-Collinear (γ-C in green circles), γ-Non-Collinear (γ-NC in blue squares) and ε-Collinear (ε in red diamonds) stand for spin states in line with Fig. 4. As a guide to the eye, the average values of all under-study for each structure γ-C (green line), γ-NC (blue line) and ε (red line) that might coexist in the experimental conditions are also shown. The energetically favoured γ-NC, γ-C and ε cases are highlighted by magenta squares. Note that the experimental values of M_S are a bit lower than the theoretical ones. This can be due, at least in part, to the formation of Ag precipitates (*i.e.*, a fraction of the Ag added to the system does not get introduced into the FeMn crystallographic structures but, instead, remains in the form of Ag precipitates). Also, bear in mind that the calculations were performed at tiny periodic unit cells and 0 K whereas the magnetic measurements are performed at room temperature.

possess different magnetic properties.

Firstly, the total crystal magnetic moment was calculated in order to compare it with the experimental data of this work. In Fig. 8(a, b) both experimental magnetization, M_S, and DFT crystal magnetic moment are enhanced with Ag content. In Fig. 8(a) the magnetic moment (μ_B/atom) is also calculated from the experimental magnetization Ms (emu g^{-1}) and the weighted g mol^{-1} percentage for FeMn – x Ag (x = 0, 1, 3, 5) %. In Fig. 8(b), the γ-FeMn crystal magnetic moment of the favored non-collinear γ-NC is zero (denoted by blue square), in agreement with previous theoretical and experimental data [35,39]. Nevertheless, the average crystal magnetic moment values of all the under-study cases in Fig. 4 are almost zero. In particular, the energetically favored ε-FeMn shows an average crystal magnetic moment of 0.065 μ_B $atom^{-1}$ (from 0 up to 0.13 μ_B $atom^{-1}$) for several configurations and spin states which might coexist in the experimental conditions.

Concerning the FeMn-6Ag wt% and FeMn-12Ag wt% alloys, the average crystal magnetic moment also depends on the spin states and structural configuration along with compositions showing, nevertheless, a small M_S increase behaviour upon Ag substitution. Namely, the average crystal magnetic moment of γ-NC and γ-C tends to increase upon Ag substitution, similar to the experimental magnetization, while the ε magnetic moment is also enhanced in ε-FeMn-6Ag. The calculated magnetic moment of the energetically favored configurations is presented in Fig. 8(b) showing the enhanced μ_B upon Ag substitution. Although there is an agreement between the present experimental data and the theoretical calculations, one should bear in mind that the DFT unit cells are tiny and cannot include dislocations or grain boundaries which might also influence the spin states and the concomitant magnetic moments. The increase of the Fe magnetic moment upon a non-magnetic element like Cu was also observed in the nanocluster cases [68].

3.4.2. Ag alters the Fe and Mn atomic magnetic moment

The Fe and Mn atomic magnetic moment of austenite and martensite structures were evaluated with and without Ag atoms. Starting with the γ-FeMn, the atomic magnetic moments stand in the range of 1.3–1.8 μ_B for the Fe (m_{Fe}) and within 1.83–2.4μ_B for the Mn (m_{Mn}) atoms, in line with previous GGA-DFT calculations [37,39]. In particular, the energetically favored 1Q collinear configuration of Fig. 4(a) has $m_{Fe} = \pm 1.56$ μ_B and $m_{Mn} = \pm 2.20$ μ_B compared to ± 1.54 μ_B and ± 2.08 μ_B, respectively, of Ref. 35 while the 3Q non-collinear spin state m_{Fe} (1.87 μ_B) and m_{Mn} (2.17 μ_B) are in line with the corresponding m_{Fe} (1.85 μ_B) and m_{Mn} (2.12 μ_B) [37]. It should be noted that, like in previous DFT studies, for all under-study cases of γ-FeMn, the atomic magnetic moment of Mn is always higher than the Fe ones. The average magnetic moment of γ-FeMn is zero for the AFM collinear 1d spin states due to the Fe-Fe and Mn-Mn nearest neighbor antiferromagnetic interactions and 0.008 μ_B $atom^{-1}$ for the noncollinear 3Q configuration while non-zero but relatively small (less than 0.06 μ_B $atom^{-1}$) values are found for the other austenite spin states. The Fe and Mn atomic magnetic moments in ε-FeMn are reduced compared to the γ-FeMn while the m_{Mn} values might be similar or even smaller than m_{Fe}. In particular, the favored FeMn [0001] AFM spin state has $m_{Fe} = 1.42$ μ_B and $m_{Mn} = -1.15$ μ_B at the ε-$Fe_{50}Mn_{50}$ and might be lowered to $m_{Fe} = 0.65$ μ_B and $m_{Mn} = -0.42$ μ_B in the relaxed DFT ε-$Fe_{50}Mn_{50}$ lattice. It should be noted that all ε-FeMn cases prefer the AFM spin states against the FM ones in line with [42]. These DFT results are in agreement with the experimentally observed magnetic moment reduction due to increase of Mn content [60] especially when co-existence of both γ and ε phases holds.

Concerning the γ-FeMn-6Ag wt%, the collinear AFM spin state becomes favoured along with the Ag preference in Mn-rich 1st neighbour environment shown in Fig. 9. Although the Ag atomic moment is virtually zero, the presence of Ag atom alters the 1Q collinear spin symmetry of the γ-FeMn system influencing the atomic magnetic moment of the Fe and Mn neighbouring atoms compared to the γ-FeMn ($m_{Fe} = \pm 1.56$ μ_B and $m_{Mn} = \pm 2.20$ μ_B), resulting in a range from 0.25 to – 1.72 μ_B for m_{Fe} and from 2.08 to 2.62 μ_B for m_{Mn} which depends on the neighbor distance and the spin direction. In particular, Ag has 12 first neighbors consisting of four Fe and eight Mn atoms. The Fe first neighbors are located in the same (001) plane with Ag and show − 1.72μ_B while upon Ag introduction they lose − 0.02 e^- per atom. In addition, due to atomic relaxation, the Ag-Fe first neighbor distance increases to 2.624 Å compared to 2.546 Å (stand for $a\frac{\sqrt{2}}{2}$, $a = 3.6$ Å experimental value used in the simulation cell) resulting in 3.1% local expansion of the Ag-Fe bonds and therefore local stress. In the third column of Fig. 9(a) the electron charge density difference is depicted along with the Ag, Fe and Mn atomic balls. The blue sphere around Ag particle denotes the Ag's spherical 5 s electron charge depletion (−0.024 e^- per atom) which also affects its first and second neighbourhood. In particular, the second Ag-Fe neighbors retain the 3.6 Å distance but they gain charge + 0.03 e^- per atom which is presented by green hemispheres in the third column. The rest of Fe neighboring atoms' distances are not affected by the Ag presence although they gain charge similar to the second neighbors. The Mn-Ag first neighbor distance is expanded by 3.4%, the atomic magnetic moment is increased to 2.62 μ_B or − 2.95 μ_B

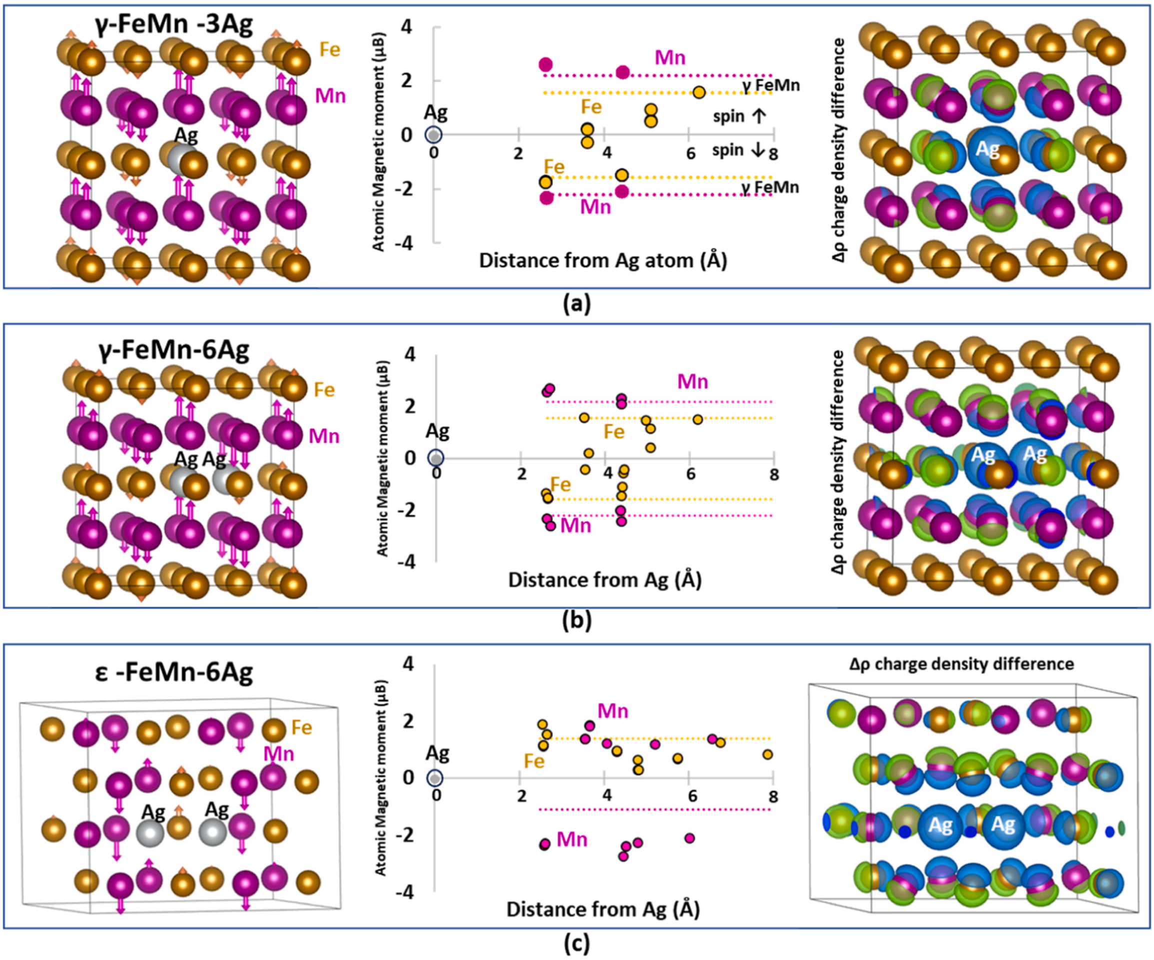

Fig. 9. FeMn-Ag atomic representation and spin state, atomic magnetic moment and electronic charge density difference: (a) γ-FeMn-6Ag wt%, (b) γ-FeMn-12Ag wt% and (c) ε-FeMn-12Ag wt%. Fe, Mn and Ag atoms are presented by gold, magenta and grey spheres. Dashed lines denote the Fe (gold) and Mn (magenta) atomic magnetic moment of γ-FeMn (in a, b) or ε-FeMn (in c). In the third column the electron charge density difference revealing charge transfer is shown along with the atomic representation, as blue spheres around Ag atoms and blue/green hemispheres with isovalue + 0.1 (for charge gain $e^-/Bohr^3$ in green) and − 0.1$e^-/Bohr^3$ (for charge lose in blue).

compared to $m_{Mn} = \pm 2.20\ \mu_B$ of the pure γ-FeMn, as shown in Fig. 9 (second column). In line with Fe, the Mn first neighbor atoms of Ag lose charge − 0.02 e^-/atom (average value on the 8 atoms presented with blue hemispheres in the third column) while the following neighbors gain charge (green hemispheres). This charge loss or gain is also illustrated in the electron charge density difference Δρ of the third column in Fig. 9 where the blue spherical area around the Ag atom denotes that the 5 s orbital main loss (−0.024 e^- per atom) also affects the neighbouring atoms. In particular, the electronic charge transfer on the Ag’s neighborhood atoms, caused by Ag, reveals electric dipole moment features on the Fe or Mn atoms having charge loss close to Ag (blue hemisphere) and charge gain away from Ag (green hemisphere) in the bond direction between Ag and all neighboring atoms.

Similar behaviour is also depicted in the case of γ-FeMn–12Ag wt% and ε-FeMn-12Ag wt%, now influencing a higher number of Ag atoms’ neighbors. In the case of ε-FeMn-12Ag wt%, the Fe (from $1.10\mu_B$ up to $1.9\mu_B$) and Mn ($-2.30\mu_B$) first neighbor atomic magnetic moments increase compared to the pure ε-FeMn ($+1.37\mu_B$ for Fe and $-1.11\mu_B$ for Mn) while the Fe next-next nearest neighbors reveal smaller atomic magnetic moment (from $0.2\mu_B$ up to $0.9\mu_B$) and slowly converge towards the ε-FeMn far from Ag atoms. The Ag-Fe first neighbor bonds are expanded from 1% up to 4% along with the Ag-Mn bonds (2%) showing the local stress introduction by Ag that might be responsible for the changes of spin states, in line with bcc Mn spin alterations due to expansion or contraction [65,66]. In addition, charge transfer is observed in the electronic charge density difference from the Ag atoms and its first neighbors (blue area indicated charge loss) towards the second and third neighbors (green hemispheres show charge gain and blue hemispheres charge loss along the Ag-neighbor atoms directions.). This Ag charge loss (0.02 e^- per atom), although small, is due to Ag’s unpair 5 s electron resulting in a positively charged Ag ion in the FeMn matrix, revealing the will of Ag to offer electrons to the system. This in turn might be related to its antibacterial properties and its ability to induce generation of reactive oxygen species [69,70]. Charge transfer between Ag and Al has been also found in the case of Ag in AlN matrix affecting the electronic properties and bonding characteristics [71].

4. Conclusions

The present study was devised to determine the effect of Ag on the phase composition and physical properties (mechanical and magnetic) of FeMn alloys. The study consisted of a variety of experimental techniques and was supported by theoretical calculations. The basic structural and magnetic properties of FeMn were reproduced in line with previous data.

This study has experimentally identified the co-existence of γ-FeMn and ε-FeMn upon Ag addition to equiatomic FeMn alloys, which is related to the decrease of the ISF energy along with the decrease in the ΔE between the two phases. The Ag atoms prefer the ISF sites, thus depleting the electron charge at the SF plane and its neighboring atomic layers, lowering the interatomic bond strength and allowing an easier slip and a possible transition from the austenite towards martensite structure. Small Ag contents in FeMn alter the well-known non-collinear FeMn spin configuration due to the modification of its nearest neighbor Fe and Mn atomic magnetic moment. In addition, Ag prefers the Mn-rich against the Fe-rich first neighborhood, affecting however both Mn and Fe nearest neighbors' atomic magnetic moment, expanding the first neighbor bond length and causing local stress. As a result, although Ag has almost zero magnetic moment, it causes a gradual increase in the FeMn magnetization.

The addition of Ag led to an increased mechanical strength of FeMn alloys at compression, which was attributed to the presence of ε-martensite as well as to precipitation strengthening. Our results could be used for the design of functionalized FeMn-Ag based alloys with targeted structures and properties, suitable for widespread technological applications.

CRediT authorship contribution statement

A.B. performed most of the experiments, helped in the interpretation of the data and wrote the first version of the manuscript. C.E.L. performed the DFT calculations. L.A.A. performed part of the expriments. I. S. performed the MFM observations. E.P. and J.S. supervised the work, helped in the interpretation of the data and revised the written manuscript.

Declaration of Competing Interest

The authors declare the following financial interests/personal relationships which may be considered as potential competing interests: Jordi Sort reports financial support was provided by European Commission. Jordi Sort reports was provided by State Agency of Research. Jordi Sort reports was provided by Government of Catalonia.

Data Availability

Data will be made available on request.

Acknowledgements

This project has received funding from the European Union's Horizon 2020 research and innovation programme under the Marie Skłodowska-Curie grant agreement No. 861046 ('Bioremia' European Training Network). Partial financial support from the Spanish Government (PID2020–116844RB-C21) and the Generalitat de Catalunya (2021-SGR-00651) is also acknowledged.

Appendix A. Supporting information

Supplementary data associated with this article can be found in the online version at doi:10.1016/j.jallcom.2023.171640.

References

[1] J.H. Schmitt, T. Iung, C. R. Phys. 19 (2018) 641–656.
[2] M. Soleimani, A. Kalhor, H. Mirzadeh, Mater. Sci. Eng. C. 795 (2020), 140023.
[3] V. Kuncser, M. Valeanu, G. Schinteie, G. Filoti, I. Mustata, C.P. Lungu, A. Anghel, H. Chiriac, R. Vladoiu, J. Bartolome, J. Magn. Magn. Mater. 320 (2008) e226–e230.
[4] T. Lin, D. Mauri, IEEE Trans. Magn. 35 (1999) 2607–2609.
[5] Z. Ma, M. Gao, D. Na, Y. Li, L. Tan, K. Yang, Mater. Sci. Eng. C. 103 (2019), 109718.
[6] H. Hermawan, A. Purnama, D. Dube, J. Couet, D. Mantovani, Acta Biomater. 6 (2010) 1852–1860.
[7] A. Bartkowska, O. Careta, A.B. Turner, A. Blanquer, E. Ibañez, M. Trobos, C. Nogués, E. Pellicer, J. Sort, Mater. Adv. 4 (2023) 616–630.
[8] Y.K. Lee, C.S. Choi, Metall. Mater. Trans. A 31 (2000) 355–360.
[9] D.T. Pierce, J.A. Jiménez, J. Bentley, D. Raabe, C. Oskay, J.E. Wittig, Acta Mater. 68 (2014) 238–253.
[10] O. Grässel, L. Krüger, G. Frommeyer, L.W. Meyer, Int. J. Plast. 16 (2000) 1391–1409.
[11] W.S. Yang, C.M. Wan, J. Mater. Sci. 25 (1990) 1821–1823.
[12] J. Fiocchi, J.N. Lemke, S. Zilio, C.A. Biffi, A. Coda, A. Tuissi, Mater. Today Commun. 27 (2021), 102447.
[13] I. Bleskov, T. Hickel, J. Neugebauer, A. Ruban, Phys. Rev. B 93 (2016), 214115.
[14] H. Gholizadeh, C. Draxl, P. Puschnig, Acta Mater. 61 (2013) 341–349.
[15] A. Abbasi, A. Dick, T. Hickel, J. Neugebauer, Acta Mater. 59 (2011) 3041–3048.
[16] Y. Hwang, S. Choi, J. Choi, S. Cho, Sci. Rep. 9 (1) (2019) 10.
[17] I. Gutierrez-Urrutia, D. Raabe, Acta Mater. 59 (2011) 6449–6462.
[18] H. Hermawan, D. Dubé, D. Mantovani, J. Biomed. Mater. Res. A 93 (2010) 1–11.
[19] H. Hermawan, Prog. Biomater. 7 (2018) 93–110.
[20] H. Hermawan, D. Dubé, D. Mantovani, Acta Biomater. 6 (2010) 1693–1697.
[21] H. Hermawan, D. Dubé, D. Mantovani, Adv. Mat. Res. 15–17 (2007) 107–112.
[22] H. Hermawan, H. Alamdari, D. Mantovani, D. Dubé, Powder Met. 51 (2008) 38–45.
[23] Y.P. Feng, A. Blanquer, J. Fornell, H. Zhang, P. Solsona, M.D. Baró, S. Suriñach, E. Ibáñez, E. García-Lecina, X. Wei, R. Li, L. Barrios, E. Pellicer, C. Nogués, J. Sort, J. Mater. Chem. B 4 (2016) 6402–6412.
[24] M.S. Dargusch, A. Dehghan-Manshadi, M. Shahbazi, J. Venezuela, X. Tran, J. Song, N. Liu, Ch Xu, Q. Ye, C. Wen, ACS Biomater. Sci. Eng. 5 (4) (2019) 1686–1702.
[25] H.J. Busscher, H.C. van der Mei, G. Subbiahdoss, P.C. Jutte, J.J.A.M. van den Dungen, S.A.J. Zaat, M.J. Schultz, D.W. Grainger, Sci. Transl. Med. 4 (2012) 153rv10.
[26] S. Daghighi, J. Sjollema, H.C. van der Mei, H.J. Busscher, E.T.J. Rochford, Biomaterials 34 (2013) 8013–8017.
[27] A.B. Lansdown, J. Wound Care 11 (2013) 125–130.
[28] S. Chernousova, M. Epple, Angew. Chem. Int. Ed. 52 (2013) 1636–1653.
[29] P. Sotoudeh Bagha, M. Khakbiz, S. Sheibani, H. Hermawan, J. Alloy. Compd. 767 (2018) 955–965.
[30] R.Y. Liu, R.G. He, Y.X. Chen, S.F. Guo, Acta Metall. Sin. Engl. Lett. 32 (2019) 1337–1345.
[31] H.A. Wriedt, W.B. Morrison, W.E. Cole, Metall. Trans. 4 (1973) 1453–1456.
[32] R.Y. Liu, R.G. He, L.Q. Xu, S.F. Guo, Acta Metall. Sin. Engl. Lett. 31 (2018) 584–590.
[33] N. Babacan, F. Kochta, V. Hoffmann, T. Gemming, U. Kühn, L. Giebeler, A. Gebert, J. Hufenbach, Mater. Today Commun. 28 (2021), 102689.
[34] A. Dehghan-Manshadi, J. Venezuela, A.G. Demir, Q. Ye, M.S. Dargusch, J. Manuf. Process. 80 (2022) 642–650.
[35] G. Kresse, J. Hafner, Phys. Rev. B 48 (1993) 13115–13118.
[36] G. Kresse, J. Furthmüller, Phys. Rev. B Condens. Matter Mater. Phys. 54 (1996) 11169–11186.
[37] D. Spišák, J. Hafner, Phys. Rev. B Condens. Matter Mater. Phys. 61 (2000) 11569–11575.
[38] J.P. Perdew, K. Burke, M. Ernzerhof, Phys. Rev. Lett. 77 (1996) 3865–3868.
[39] M. Ekholm, I.A. Abrikosov, Phys. Rev. B Condens. Matter Mater. Phys. 84 (2011), 104423.
[40] H.C. Herper, E. Hoffmann, P. Entel, Phys. Rev. B Condens. Matter Mater. Phys. 60 (1999) 3839–3848.
[41] D.E. Jiang, E.A. Carter, Phys. Rev. B Condens. Matter Mater. Phys. 67 (2003), 214103.
[42] J.S. Kouvel, J.S. Kasper, J. Phys. Chem. Solids 24 (1963) 529–536.
[43] V.T. Witusiewicz, F. Sommer, E.J. Mittemeijer, J. Phase Equilibria Diffus. 25 (2004) 346–354.
[44] Y.K. Lee, J.H. Jun, C.S. Choi, ISIJ Int 37 (1997) 1023–1030.
[45] C.M. Li, F. Sommer, E.J. Mittemeijer, Mater. Sci. Eng. A 325 (2002) 307–319.
[46] P. Marinelli, A. Baruj, A. Fernández Guillermet, M. Sade, Z. Metall. 92 (2001) 489–493.
[47] P. Singh, S. Picak, A. Sharma, Y.I. Chumlyakov, R. Arroyave, I. Karaman, D. D. Johnson, Phys. Rev. Lett. 127 (2021), 115704.
[48] J. Dash, H.M. Otte, Acta Met. 11 (1963) 1169–1178.
[49] S. Takaki, H. Nakatsu, Y. Tokunaga, Mater. Trans. JIM 34 (1993) 489–495.
[50] G. Parr, J. Iron Steel Inst. 171 (1952) 137–141.
[51] A. Dick, T. Hickel, J. Neugebauer, Steel Res. Int. 80 (2009) 603–608.
[52] X. Cui, J. Wang, H. Wang, X.G. Lu, J. Jiang, Met. Mater. Int. 28 (2022) 1215–1223.
[53] B.C. De Cooman, Y. Estrin, S.K. Kim, Acta Mater. 142 (2018) 283–362.
[54] D.T. Pierce, J.A. Jiménez, J. Bentley, D. Raabe, J.E. Wittig, Acta Mater. 100 (2015) 178–190.
[55] R.Y. Liu, R.G. He, L.Q. Xu, S.F. Guo, Acta Metall. Sin. Engl. Lett. 31 (2018) 584–590.
[56] D. Carluccio, C. Xu, J. Venezuela, Y. Cao, D. Kent, M. Bermingham, A.G. Demir, B. Previtali, Q. Ye, M. Dargusch, Acta Biomater. 103 (2020) 346–360.
[57] M. Heiden, E. Nauman, L. Stanciu, Adv. Healthc. Mater. 6 (2017) 1700120.
[58] P. Liu, D. Zhang, Y. Dai, J. Lin, Y. Li, C. Wen, Acta Biomater. 114 (2020) 485–496.
[59] Y. Ishikawa, Y. Endoh, J. Appl. Phys. 39 (2003) 1318.
[60] Y. Endoh, Y. Ishikawa, J. Phys. Soc. Jpn. 30 (2013) 1614–1627.
[61] H. Umebayashi, Y. Ishikawa, J. Phys. Soc. Jpn. 21 (1966) 1281–1294.
[62] P. Bisanti, G. Mazzone, F. Sacchetti, J. Phys, F 17 (1987) 1425–1435.
[63] S.J. Kennedy, T.J. Hicks, J. Phys, F 17 (1987) 1599–1604.
[64] S. Kawarazaki, Y. Sasaki, K. Yasuda, T. Mizusaki, A. Hirai, J. Phys. Condens. Matter 2 (1990) 5747–5752.
[65] S. Fujii, S. Ishida, S. Asano, J. Phys. Soc. Jpn. 60 (1991) 4300–4310.
[66] N.E. Brener, G. Fuster, J. Callaway, J.L. Fry, Y.Z. Zhao, J. Appl. Phys. 63 (1988) 4057–4059.
[67] N.I. Medvedeva, D. van Aken, J.E. Medvedeva, J. Phys. Condens. Matter 22 (2010), 316002.
[68] C.S. Cutrano, C.E. Lekka, J. Alloy. Compd. 707 (2017) 114–119.

[69] M. Dhanalakshmi, S. Thenmozhi, K. Manjula Devi, S. Kameshwaran, Int. J. Pharm. Biol. Arch. 4 (2013) 819–826.

[70] T. Ishida, MOJ Toxicol. 4 (2018) 345–350.

[71] Ch.E. Lekka, P. Patsalas, Ph Komninou, G.A. Evangelakis, J. Appl. Phys. 109 (2011), 054310.